ChemElectroChem

Research Article
doi.org/10.1002/celc.202200374

Chemistry Europe
European Chemical Societies Publishing

www.chemelectrochem.org

Scalable Composites Benefiting from Transition-Metal Oxides as Cathode Materials for Efficient Lithium-Sulfur Batteries

Vittorio Marangon,[a] Eugenio Scaduti,[b] Viviana Fatima Vinci,[b] and Jusef Hassoun*[a, b, c]

Composite materials achieved by including transition-metal oxides with different structures and morphologies in sulfur are suggested as scalable cathodes for high-energy lithium-sulfur (Li–S) batteries. The composites contain 80 wt.% sulfur and 20 wt.% of either MnO_2 or TiO_2, leading to a sulfur content in the electrode of 64 wt.% and revealing a reversible, fast, and lowly polarized conversion process in the cell with limited interphase resistance. The S–TiO_2 composite exhibits an excellent rate capability between C/10 and 2C, and a cycle life extended over 400 cycles at 2C, owing to the effects of the nanometric TiO_2 additive in boosting the reaction kinetics. Instead, the micrometric sized particles of MnO_2 partially limit the electrochemical activity of S–MnO_2 to the current rate of 1C. Nevertheless, both S–MnO_2 and S–TiO_2 withstand a sulfur loading up to values approaching 6 mg cm^{-2}, and deliver an areal capacity ranging from about 4.5 to 5.5 mAh cm^{-2} at C/5. The excellent performances of the metal oxide-sulfur electrodes, even at high active material loading, and the possible scalability of the synthetic pathway adopted in the work suggest that the composites are viable cathodes for next-generation Li–S batteries with high energy density and efficient electrochemical process.

Introduction

Recent concerns raised by the global climate change triggered the development of new energy storage technologies to actually promote the large-scale diffusion of sustainable transport systems, such as electric vehicles (EVs), with satisfactory autonomy.[1–3] The present technology of choice to power most of the electronic devices is the rechargeable lithium-ion battery, that relies on the reversible (de)intercalation of Li^+ ions into and from electrodes typically with a layered structure.[4] Despite the notable progress achieved by intensive research work, challenges in the Li-ion technology such as the relatively limited energy content, the environmental and economic impact of the materials, and the need for an efficient recycling process still hinder a complete transition to a zero-emission mobility.[5] In this scenario, rechargeable lithium-sulfur (Li–S) battery may represent an alternative system due the low cost of sulfur, and the high theoretical energy associated with the multi-electron electrochemical conversion reaction summarized by equation (1):[6]

$$16Li^+ + S_8 + 16e^- \rightleftharpoons 8Li_2S \quad (1)$$

This intriguing process can in fact deliver an energy density of 3730 Wh kg^{-1} as referred to the sulfur mass, that may lead to a practical value exceeding 400 Wh kg^{-1}, thus remarkably improving the one ascribed to the Li-ion which typically ranges from 250 Wh kg^{-1} to about 300 Wh kg^{-1}.[6–8] These appealing features have boosted relevant research efforts towards the Li–S technology for addressing the several issues that still prevent its practical and large-scale diffusion.[9–11] Among the various drawbacks affecting the Li–S battery, the most severe may be ascribed with the possible reactivity of the polysulfide intermediates formed during Li–S conversion process (Li_2S_x, $2 \leq x \leq 8$) with the anode. Indeed, the soluble fraction of these species formed during discharge (typically Li_2S_8 and Li_2S_6) can migrate through the electrolyte to undergo direct reduction at the lithium metal surface, and subsequently diffuse back to the cathode to be newly oxidized during charge. This "shuttle process" between the electrodes typically leads to an apparent charge without any energy storage, with active material loss, anode degradation, low coulombic efficiency, and capacity fading.[12,13] Several approaches have been undertaken to control the undesired processes ascribed to the soluble polysulfides during battery operation, including the use of sulfur-carbon composites,[14–17] inorganic cathode additives,[18–20] alternative binders,[21,22] polymer electrolytes,[23,24] electrolyte sacrificial agents,[25–27] as well as functional interlayers[28,29] and separators.[30,31] In particular, transition metal oxides of various nature and morphology have been thoroughly studied for

[a] Dr. V. Marangon, Prof. J. Hassoun
Graphene Labs, Istituto Italiano di Tecnologia
via Morego 30, Genova, 16163, Italy
E-mail: jusef.hassoun@iit.it
[b] E. Scaduti, V. F. Vinci, Prof. J. Hassoun
Department of Chemical, Pharmaceutical and Agricultural Sciences, University of Ferrara
Via Fossato di Mortara 17, Ferrara, 44121, Italy
[c] Prof. J. Hassoun
National Interuniversity Consortium of Materials Science and Technology (INSTM), University of Ferrara Research Unit
Via Fossato di Mortara, 17, 44121, Ferrara, Italy
E-mail: jusef.hassoun@unife.it

Supporting information for this article is available on the WWW under https://doi.org/10.1002/celc.202200374

possibly mitigating the polysulfides diffusion into the electrolyte, and improving of the Li–S cell behavior. The favorable effects of metal oxide additives have been attributed to the strong polar interactions between the electron attractive metal nuclei with the negatively charged sulfur (S_x^{-2}), and of the oxygens with the Li^+ ions.[32–35] Among the various oxides, those based on Mn and Ti have received particular attention from the scientific community due to their exceptional polysulfides restraining ability.[32–35] Furthermore, the development of sustainable sulfur composite cathodes[36–38] and the implementation of scalable synthesis procedures appeared as very promising approaches for limiting the economic impact and actually achieving a practical Li–S battery.[39] Promising recent works revealed remarkable Li–S performances based on metal oxides having particular morphologies obtained through alternative synthesis pathways, such as three-dimensional porous MnO_2[40] and room-like TiO_2[41] as hosts for sulfur. In this work, we use the sustainable and environmentally friendly sulfur with transition metal oxides to achieve high-performance composites for lithium battery, through a simple and straightforward physical mixing pathway. Hence, commercial MnO_2 and TiO_2 powders are employed without additional synthetic steps as advantageous additives in sulfur composites with a weight ratio of the active material as high as 80%. Electrochemical tests are preliminarily carried out on the MnO_2 and TiO_2 materials to exclude possible side activity of the oxides which may affect the Li–S conversion process. Subsequently, the corresponding sulfur composites cast on porous carbon current-collector of suitable electrical conductivity are employed as the positive electrode in efficient lithium cells.[42,43] Hence, we propose herein a possible strategy to achieve improved electrodes, and possibly scale up a high-energy Li–S battery.

Results and Discussion

Structure, morphology and possible side electrochemical activity of the metal oxide additive may actually play a crucial role in determining the cell performance of the corresponding sulfur composites.[32–35] Therefore, MnO_2 and TiO_2 powders are initially investigated by X-ray diffraction (XRD) as shown in Figure S1a, b (Supporting Information). The corresponding patterns reveal a well-defined crystalline structure for both the metal oxides, identified by β-phase (pyrolusite) for MnO_2 (Figure S1a) with the $P4_2/mnm$ space group, and α phase (anatase) for TiO_2 (Figure S1b) with the $I4_1/amdZ$ space group.[44,45] The absence of significant impurities in the XRD patterns suggest the suitability of the oxides for electrochemical application. The morphological features of MnO_2 and TiO_2 are provided by the scanning electron microscopy (SEM) images reported in Figure S1(c, e and g) for MnO_2 and in Figure S1(d, f and h) for TiO_2. The metal oxide powders exhibit substantial differences in morphology: indeed, MnO_2 shows particles with defined flake-like geometry and irregular sizes ranging from sub-micrometric values to about 3 μm (Figure S1c, e and g), instead TiO_2 powder is homogeneously formed by nanometric crystals smaller than 500 nm (Figure S1d, f and h). It is worth mentioning that large MnO_2 particles can possibly hinder the electrolyte decomposition in the lithium cell, while the smaller domains typically boost the kinetics of the electrochemical reactions and favor the discharge and charge processes.[46] On the other hand, the nanometric size observed for the TiO_2 particles are particularly suggested to shorten the diffusion path and improve the kinetics of the electrochemical processes. However, excessively small particles typically induce electrolyte decomposition and raise the electrode/electrolyte interphase resistance in particular at increased anodic potentials.[47] A more detailed study on the particle size of MnO_2 and TiO_2 is provided by the transmission electron microscopy (TEM) images displayed in panels (a, c) and (b, d) of Figure S2 (Supporting Information), respectively, which were acquired upon samples sonication (see experimental section). The analyses confirm the vast size range of the MnO_2 flakes, extending from 50 nm to 3 μm, and show wide TiO_2 clusters composed of quasi-spherical primary particles with dimensions from 50 to 200 nm. The electrochemical characteristics of MnO_2 and TiO_2 in lithium cell are then investigated by cyclic voltammetry (CV), galvanostatic cycling and electrochemical impedance spectroscopy (EIS) with outcomes displayed in Figure 1. The voltammogram related to the MnO_2 electrode (Figure 1a) shows during the first cycle reduction with a peak centered at about 2.7 V *vs.* Li^+/Li during the cathodic scan, and oxidation at about 3.2 V *vs.* Li^+/Li during the reverse anodic scan as likely due to the electrochemical process reported in equation (2):[48]

$$x\mathrm{Li}^+ + \mathrm{MnO_2} + xe^- \rightleftharpoons \mathrm{Li}_x\mathrm{MnO_2}\ [49] \quad (2)$$

The subsequent CV curves become more symmetric, overlap, and indicate a redox process centered at about 3 V *vs.* Li^+/Li, while the anodic current slightly improves. The observed changes typically suggest a structural reorganization of the electrode upon the electrochemical process, and the concomitant formation of a solid electrolyte interphase (SEI) layer at the electrodes surface, which may affect the Li^+ exchange.[50,51] It is worth mentioning that the relatively low current value for the peaks observed in the voltammogram of Figure 1a, i.e., with a maximum value approaching 60 μA using an electrode with geometric area of 0.785 cm^2, suggests a poor electrochemical activity of the bare MnO_2. On the other hand, TiO_2 exhibits CV signals (Figure 1b) with cathodic peak centered at about 1.7 V *vs.* Li^+/Li, and a subsequent anodic one at about 2.1 V *vs.* Li^+/Li which identify the (de)insertion process displayed in equation (3):[52]

$$x\mathrm{Li}^+ + \mathrm{TiO_2} + xe^- \rightleftharpoons \mathrm{Li}_x\mathrm{TiO_2} \quad (3)$$

Despite the higher currents for TiO_2 compared to MnO_2 during the first CV cycle, with anodic and cathodic values of 200 and −400 μA, respectively, Figure 1b reveals a very fast decay during the subsequent cycles, thus suggesting a progressive hindering of the corresponding redox process. In order to further characterize the electrochemical features of the two oxides, galvanostatic cycling tests using them as the working electrodes in lithium cell are performed at the current

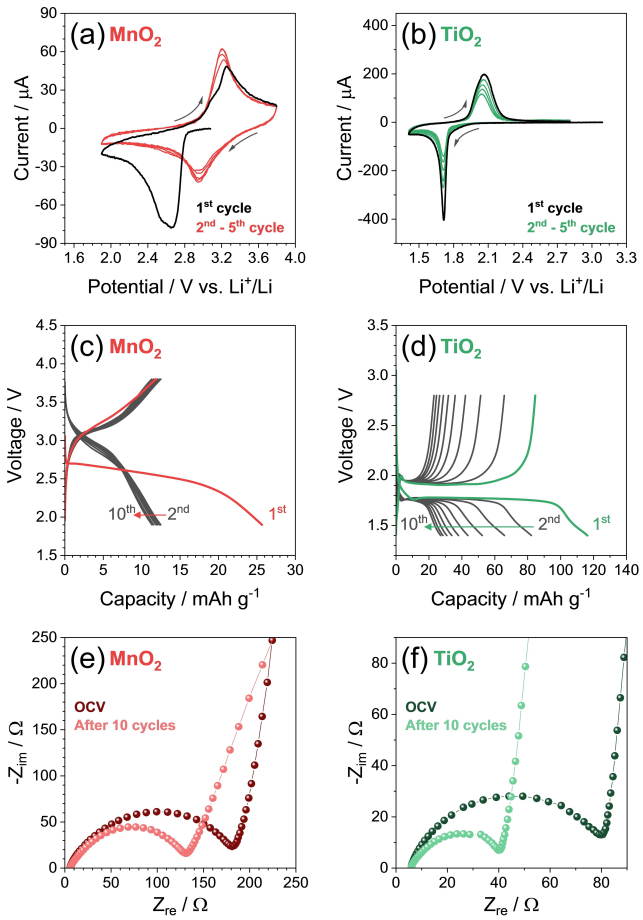

Figure 1. Electrochemical behavior of a, c, e) MnO_2 and b, d, f) TiO_2 electrodes in lithium cell with the configuration Li | EC:DMC 1 : 1 V : V, 1 M $LiPF_6$ | cathode. In particular: a, b) CV measurements performed at the scan rate of 0.1 mV s^{-1} between 1.9 and 3.8 V *vs.* Li^+/Li for MnO_2 and from 1.4 to 2.8 V *vs.* Li^+/Li for TiO_2; c, d) voltage profiles related to galvanostatic cycling of the lithium cells at the constant current rate of C/10 in the 1.9–3.8 V and 1.4–2.8 V voltage ranges for MnO_2 (1C = 308 mA g^{-1}) and TiO_2 (1C = 168 mA g^{-1}), respectively; e, f) Nyquist plots recorded through EIS carried out on the lithium cells at the OCV condition and upon 10 discharge/charge cycles. Frequency range: 500 kHz–10 mHz. Alternate voltage signal amplitude: 10 mV. Room temperature (25 °C).

rate of C/10 (1C = 308 mA g^{-1} for MnO_2 and 168 mA g^{-1} for TiO_2). The corresponding voltage profiles reported in Figure 1(c, d) fit with the CV curves, and show for the MnO_2 electrode (Figure 1c) a first cycle characterized by a single discharge plateau evolving at 2.6 V and charge processes centered at 3.3 V, that shift to 2.9 and 3.2 V, respectively, in the subsequent cycles due to the above mentioned structural modification of the material and SEI film formation on the electrodes surface.[51] Relevantly, Figure 1c evidences a very poor delivered capacity for the material with a value limited to 26 mAh g^{-1} during the first discharge, decreasing to 12 mAh g^{-1} during the subsequent cycles, as above suggested by the modest CV currents. As for the cell performance of TiO_2 electrode, Figure 1d shows flat profiles typical of the biphasic (de)insertion process, with discharge taking place at 1.8 V and charge at 1.9 V,[51,52] and corresponding capacities of 120 and 80 mAh g^{-1}, respectively, during the first cycle. Subsequently, the delivered capacity of the Li | TiO_2 cell (Figure 1d) rapidly drops to reach a value of about 27 mAh g^{-1} at the 10th cycle, thus confirming the limits of the electrochemical process already shown by CV in Figure 1b. Despite the low capacity values delivered by the MnO_2 and TiO_2 electrodes through cycling, the suitable stability of the electrode/electrolyte interphase in lithium cell is a very important parameter to be evaluated for a possible application of the two oxides as additives in sulfur composites. Therefore, Nyquist plots have been recorded through EIS at the open circuit voltage (OCV) condition of the lithium cells and after 10 discharge/charge cycles and reported in Figure 1e and f. The obtained results are analyzed through the non-linear least squares (NLLS) fitting method, throughout a Boukamp software that allows the evaluation of the various resistance contributes by building an equivalent circuit formed by resistances indicated by (R) and constant phase elements (CPE) indicated by (Q).[53,54] Table 1, including the outcomes of the NLLS analyses, reveals that the cells fit with the $R_e(R_iQ_i)Q_g$ circuit in which R_e is the electrolyte resistance identified by the high-frequency intercept of the semicircle, R_i in the (R_iQ_i) element is the electrode/electrolyte interphase resistance corresponding to the width of the high-medium frequency semicircle with contributions of charge transfer and SEI layer, while Q_g indicates the geometric capacity of the cell represented by a low frequency tilted line.[53,54] The NLLS analyses in Table 1 evidence relatively limited R_i values for both MnO_2 (Figure 1e) and TiO_2 (Figure 1f), which become even lower upon cycling in lithium cell. In particular, the electrode/electrolyte interphase resistance related to MnO_2 drops from 186 Ω at the OCV condition to 131 Ω after 10 cycles, while that of TiO_2 decreases from 77 to 37 Ω. Relevantly, TiO_2 exhibits lower resistance values with respect to MnO_2 likely due to the nanometric morphology of the sample (see Figure S1 in the Supporting Information) which causally leads to a more conductive SEI with favorable ion exchange.[47] The low resistance values observed in Table 1 and the structural stability of the SEI suggested by the evolution of the Nyquist plots in Figure 1(e, f) indicate a possible applicability of the two metal oxides in the sulfur composite,[55] despite the very modest contribution expected by the (de)insertion process to the overall capacity of the Li/S cell.

In summary, the analyses of the MnO_2 and TiO_2 materials displayed in Figures S1, S2 and in Figure 1 show different structure and morphology, as well as a stable electrode/electrolyte interphase and a poor intrinsic electrochemical contribution, thus suggesting the employment of these metal oxides in Li–S battery as an "almost inert" cathode additive, however with a possible active role in boosting the conversion reaction, increasing the lithium polysulfides retention, and

Table 1. Non-linear least squares (NLLS) analyses performed through the Boukamp software on the Nyquist plots reported in Figure 1.[53,54]

Material	Cell condition	Circuit	R_i [Ω]	χ^2
MnO_2	OCV	$R_e(R_iQ_i)Q_g$	186 ± 1	3×10^{-4}
	After 10 cycles	$R_e(R_iQ_i)Q_g$	131 ± 1	5×10^{-4}
TiO_2	OCV	$R_e(R_iQ_i)Q_g$	77.2 ± 0.3	9×10^{-5}
	After 10 cycles	$R_e(R_iQ_i)Q_g$	37.1 ± 0.4	7×10^{-4}

mitigating their shuttle process.[32] The ability of retaining lithium polysulfides intermediates formed during Li–S conversion is qualitatively shown through photographic images in Figure S3 (Supporting Information) and Figure 2a, and actually evaluated by UV-vis measurements in Figure 2b. Vials containing MnO_2 and TiO_2 samples are prepared (Figure S3a) and filled with an electrolyte solution composed of 1,3-dioxolane (DOL) and 1,2-dimethoxyethane (DME) dissolving LiTFSI and $LiNO_3$, added with an amount of 0.5 wt.% of Li_2S_8 polysulfide (see preparation details in Experimental section). The pristine polysulfide-added electrolyte exhibits a dark red color due to the presence of Li_2S_8 (Figure S3b, left-hand side), which is strongly mitigated upon direct contact with MnO_2 (Figure S3b, center), and partly reduced by TiO_2 powder (Figure S3b, right-hand side) already after 90 minutes since addition. The difference in color is further evidenced in Figure 2a, which shows the solutions collected upon 5 hours of aging in the respective vials. The softening of the dark red color is ascribed to the partial polysulfides retention by the transition metal oxides, which is particularly effective for MnO_2 as suggested by the light color of the related solution.[56] The better polysulfides retention of MnO_2 is confirmed by the UV-vis measurements performed on the pristine Li_2S_8-added electrolyte, and on the solutions held in contact with MnO_2 and TiO_2 as reported in Figure 2b. Indeed, the analyses show a characteristic signal of lithium polysulfide species in the visible region between 750 and 550 nm for all the three solutions.[57] The pristine Li_2S_8-added solution exhibits the expected intense response, whilst the solution held in contact with TiO_2 displays a lower polysulfide signal that almost vanishes for the one using MnO_2 (Figure 2b). Therefore, the selected transition metal oxides actually reveal a lithium polysulfide retention ability, which may be influenced by the intrinsic interactions between MnO_2 and TiO_2 and Li_2S_x species, as well as by the different morphology of the two samples (see Figure S1 in Supporting Information). Consequently, a different cycling behavior of the S–MnO_2 and S–TiO_2 composites is

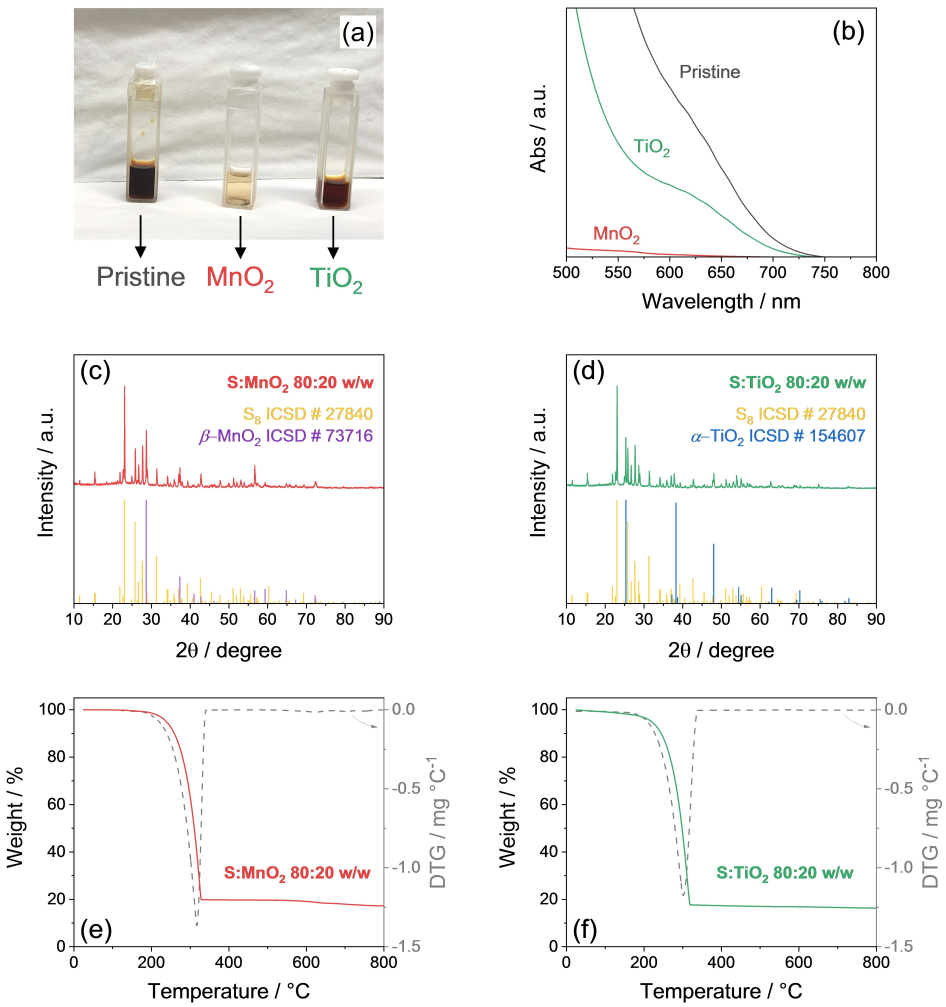

Figure 2. a) Samples of the DOL:DME, 1 mol kg^{-1} LiTFSI, 1 mol kg^{-1} $LiNO_3$ electrolyte solution added with the 0.5 wt.% of Li_2S_8 (see Experimental section for preparation details) either at the pristine state (left-hand side), or upon 5 hours aging in contact with MnO_2 (center) and TiO_2 (right-hand side), additional images are reported in Figure S3 (Supporting Information). b) UV-vis measurements performed on the Li_2S_8-containing solutions displayed in panel (a) in the 500–800 nm wavelength range by using a DOL:DME 1:1 *w/w* solution as reference. XRD patterns of the c) S–MnO_2 and d) S–TiO_2 sulfur-metal oxide composites, reference data for orthorhombic sulfur (S_8, ICSD #27840, yellow), manganese oxide (β-MnO_2, ICSD #73716, violet) and titanium oxide (α-TiO_2, ICSD #154607, blue) are also reported. TGA and corresponding DTG carried out on the e) S–MnO_2 and f) S–TiO_2 composites between 25 and 800 °C under N_2 flow at an increasing temperature of 5 °C min^{-1}. See experimental section for acronyms.

expected in lithium cell. The structure of the S–MnO_2 and S–TiO_2 composites is determined through XRD. The resulting patterns of S–MnO_2 (Figure 2c) and S–TiO_2 (Figure 2d) exclusively show the orthorhombic sulfur (S_8) and the corresponding metal oxide signals, that is, β–MnO_2 and α–TiO_2. The crystallographic data indicate the adequateness of the mild synthesis condition adopted herein for achieving a suitable physical mixing between sulfur and the metal oxide, without any side reaction that can possibly lead to the formation of additional and undesired compounds, as indeed suggested by our previous works for different composites.[58–60] The accurate determination of the sulfur content in the composites is achieved by the thermogravimetric analyses (TGA) and the corresponding differentiate thermogravimetry (DTG) reported in Figure 2e for S–MnO_2 and Figure 2f for S–TiO_2. Indeed, the measurements exhibit a single weight drop centered at 300 °C ascribable to sulfur evaporation[61] that corresponds to a sulfur loading of 80 % in both S–MnO_2 and S–TiO_2. Thus, the analyses evidence that the facile synthesis pathway adopted herein avoid sulfur loss through evaporation and allows the tuning of high amounts of sulfur in composites designed for high energy density lithium batteries.

This synthetic pathway, that may be reasonably scaled to achieve practical production, does not affect the metal oxides morphology, and leads to their uniform distribution into the composites as determined by SEM coupled with X-ray energy dispersive spectroscopy (EDS) (Figure 3a–j). The SEM-EDS analyses reveal large sulfur domains (up to 20 μm) homogenously decorated with either micrometric MnO_2 (Figure 3a–e) or with nanosized TiO_2 (Figure 3f–j), that is, sulfur including metal oxides with similar morphology to that of bare materials observed in Figure S1. The main morphological difference observed for the two composites, which is principally ascribed to the additives, is reasonably expected to differently influence their electrochemical behavior in Li–S battery as will be shown hereafter.

The composites are then employed in lithium cell and investigated through CV and EIS as reported in Figure 4. The voltammograms related to the Li|S–MnO_2 and Li|S–TiO_2 cells are displayed in Figure 4a and Figure 4b, while the corresponding Nyquist plots acquired through EIS at the OCV condition and after 1, 5 and 10 CV cycles are displayed in Figure 4c and Figure 4d, respectively. The first CV cycle shows for both the S–Metal oxide electrodes a reversible conversion process, indicated by the two reduction peaks at about 2.28 and 2.0 V *vs.* Li^+/Li during the cathodic scan, which are reversed into a double oxidation signal extending from 2.3 to 2.5 V *vs.* Li^+/Li during the subsequent anodic scan. This response is in line with the multi-step electrochemical process leading to the formation of lithium polysulfides with various chain length during discharge, namely, Li_2S_8, Li_2S_6 and subsequently Li_2S_x with $2 \leq x \leq 4$, which are conversed back to Li and S upon charge.[62] It is worth noting that the narrow peaks exhibited by the two voltammograms, and the overlapping of the subsequent potential profiles actually suggest adequate kinetics and

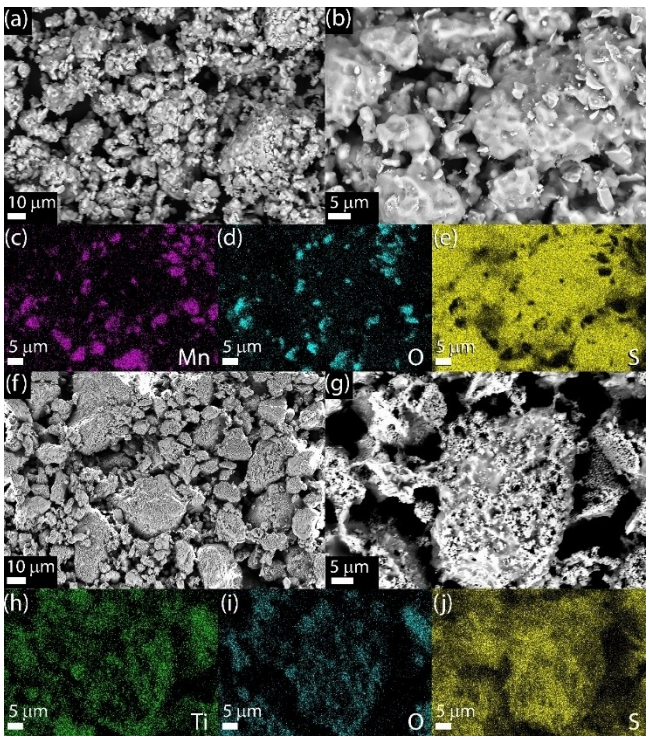

Figure 3. SEM images of the a, b) S–MnO_2 and f, g) S–TiO_2 composites with corresponding EDS elemental maps in panels (c–e) and (h–j), respectively, showing distribution of c) manganese, h) titanium, d, i) oxygen, and e, j) sulfur. See the Experimental Section for acronyms.

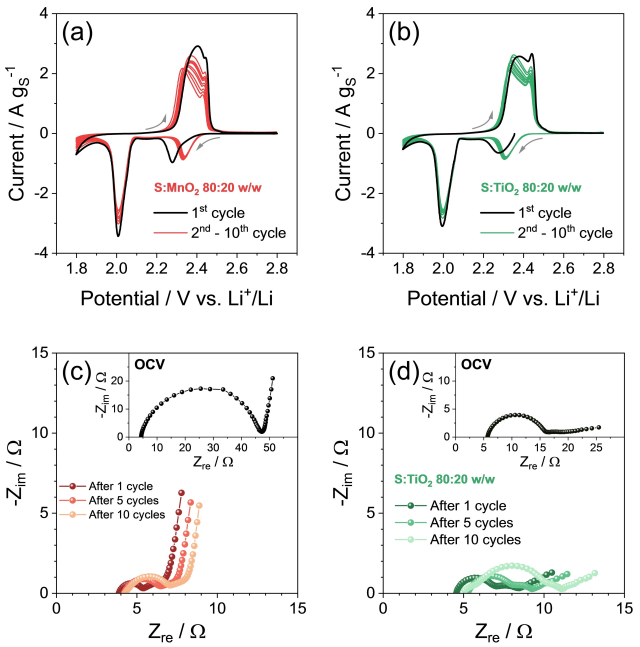

Figure 4. Electrochemical behavior of the a, c) S–MnO_2 and b, d) S–TiO_2 composites in lithium cell with the configuration Li|DOL:DME, 1 mol kg^{-1} LiTFSI, 1 mol kg^{-1} $LiNO_3$|cathode. In particular: a, b) CV profiles with current normalized to sulfur mass in the electrode at the scan rate of 0.1 mV s^{-1} in the 1.8–2.8 V *vs.* Li^+/Li potential range; c, d) Nyquist plots recorded through EIS carried out on the lithium cells at the OCV condition (inset) and after 1, 5 and 10 CV cycles. Frequency range: 500 kHz–100 mHz. Alternate voltage signal amplitude: 10 mV. Sulfur loading: ~1.5 mg cm^{-2} (electrode geometric area: 1.54 cm^2). Electrolyte/sulfur (E/S) ratio: 15 μl mg^{-1}. Room temperature (25 °C). See the Experimental Section for acronyms.

stability of the electrochemical reaction, despite the slight decrease of the peak current upon scanning may imply minor losses of active material. Furthermore, the exclusive presence of the potential signature ascribed to the Li–S conversion process, without any additional CV peak, confirms the negligible contribute of the electrochemical (de)insertion reaction of MnO_2 and TiO_2, as already speculated during the discussion of Figure 1. On the other hand, the shift of the discharge signal centered at 2.28 V *vs.* Li^+/Li to higher potential values, that is, 2.33 V *vs.* Li^+/Li for S–MnO_2 (Figure 4a) and 2.31 V *vs.* Li^+/Li for S–TiO_2 (Figure 4b) observed upon the first cycle indicates the decrease of the discharge/charge polarization. This *activation* is associated with the improvement of the electrode/electrolyte interphase conductivity due to the stabilization of an adequate SEI layer, and the advantageous migration by electrodeposition of the insulating sulfur from the surface of the porous carbon current-collector to its bulk which, in turn, enhances the electrical contact of the active material with the conductive matrix and promotes the ion transport in the interphase as demonstrated in previous works.[59,60] The increase of electrode conductivity is well confirmed by the Nyquist plots recorded upon CV (Figure 4c, d), which are analyzed by NLLS fitting method and the results are reported in Table 2.[53,54] Both Li–S cells show a decrease of the interphase resistance (R_i) upon cycling, from values of 24 Ω for S–MnO_2 and 14 Ω for S–TiO_2 at the OCV condition, to 6 Ω and 5 Ω, respectively, after 10 CV cycles. On the other hand, the NLLS analyses of Table 2 reveal differences in the equivalent circuits of the two Li–S systems. Indeed, the Nyquist plots of the Li|S–TiO_2 cell (Figure 4d) show at low frequencies a line tilted at about 45° which is typical of a Warburg-type semi-infinite Li^+ diffusion, indicated by the CPE (Q_w) in the corresponding equivalent circuit.[63] Instead, the low frequency region of the Li|S–MnO_2 cell (Figure 4c) evidences the presence of an almost vertical line attributed to the geometric capacity in a quasi-blocking electrode setup, indicated by the CPE (Q_g) in the corresponding equivalent circuit of Table 2. It is worth mentioning that the number of the (R_iQ_i) elements in the circuits of Table 1 varies by the ongoing of the CV test due to the progressive and favorable modification of the electrode/electrolyte interphase.[59,60]

Further electrochemical characteristics of the two materials are provided by the rate capability tests in Figure 5, carried out on the Li|S–MnO_2 and Li|S–TiO_2 cells at the increasing currents of C/10, C/8, C/5, C/3, C/2, 1C and 2C (1C = 1675 mA g_S^{-1}). The voltage profile of S–MnO_2 (Figure 5a) and of S–TiO_2 (Figure 5b) show at C/10 two distinct discharge plateaus evolving at about 2.3 and 2.1 V and charge plateaus merging between 2.2 and 2.4 V, thus accounting for the reversible conversion of Li and S to lithium polysulfides (Li_2S_x with $2 \leq x \leq 8$) in full agreement with the CV response discussed in Figure 4. Moreover, the voltage profiles reveal a low polarization between the discharge and charge processes that slightly grows at higher C-rates due to the increasing ohmic drop triggered by raising the current. In spite of the similarity and the adequateness of the Li|S–MnO_2 and the Li|S–TiO_2 cell responses at current ranging from C/10 to 1C, the S–MnO_2 electrode reveals a poor behavior at the relatively high current rate of 2C (Figure 5a), instead the S–TiO_2 well operates at the same C-rate (Figure 5b). This aspect is further evidenced by the corresponding cycling trends: hence, S–MnO_2 (Figure 5c) delivers capacity values of 1060, 1030, 990, 930, 870 and 780 mAh g_S^{-1} at the C/10, C/8, C/5, C/3, C/2 and 1C rates, respectively, that drop to 160 mAh g_S^{-1} at 2C, while S–TiO_2 shows a discharge capacity of 1100, 1060, 1030, 990, 940 and 870 mAh g_S^{-1} from C/10 to 1C, and still delivers a value of 790 mAh g_S^{-1} at 2C, thus suggesting a better rate capability for the latter compound with respect to the former. The above difference may be attributed to specific effects on the kinetics of the Li–S conversion promoted by the nanometric TiO_2 and the micrometric MnO_2. Indeed, the notable lithium polysulfides retention ability of the MnO_2 may possibly slow down the Li–S conversion and limit the rate capability,[24] while the nanometric morphology of the TiO_2 (Figure S1 in Supporting Information) may actually boost the electrode kinetics and the cycling rate of the cell. On the other hand, both materials recover almost completely the pristine electrochemical response upon lowering the C-rate back to C/10 after 35 cycles, as S–MnO_2 delivers 995 mAh g_S^{-1} and S–TiO_2 1050 mAh g_S^{-1} that correspond to about 95% of the respective initial capacity. These notable performances indicate an outstanding capacity retention upon the stress caused by raising the current, likely ascribed to the polysulfide-retaining ability of the metal oxides in the composite sulfur cathode, and a rate capability particularly favored by the nanometric morphology.[32,35,64]

Figure 6 reports the cycling trends related to the prolonged galvanostatic cycling tests at fixed current rates, that is, C/5 (Figure 6a), 1C (Figure 6b) and 2C (Figure 6c), performed to evaluate the cycle life of the Li–S cells. The two sulfur-metal oxide composites show adequate cycle life, extended over 120 cycles at the rate of C/5 (Figure 6a) and 1C (Figure 6b), with promising delivered capacity values, suitable capacity retention,

Table 2. Non-linear least squares (NLLS) analyses performed through the Boukamp software on the Nyquist plots reported in Figure 2.[53,54]

Material	Cell condition	Equivalent Circuit	R_1 [Ω]	R_2 [Ω]	R_3 [Ω]	R_i ($\sum R_n$) [Ω]	χ^2
S:MnO_2 80:20 w/w	OCV	$R_e(R_1Q_1)(R_2Q_2)Q_g$	22.5 ± 0.1	1.9 ± 0.4	/	24.4 ± 0.5	5×10^{-5}
	After 1 CV cycle	$R_e(R_1Q_1)(R_2Q_2)Q_g$	5.1 ± 0.3	1.8 ± 0.5	/	6.9 ± 0.8	8×10^{-5}
	After 5 CV cycles	$R_e(R_1Q_1)(R_2Q_2)Q_g$	5.8 ± 0.2	0.4 ± 0.1	/	6.2 ± 0.3	3×10^{-5}
	After 10 CV cycles	$R_e(R_1Q_1)(R_2Q_2)(R_3Q_3)Q_g$	1.4 ± 0.2	3.9 ± 0.3	0.6 ± 0.1	5.9 ± 0.6	1×10^{-5}
S:TiO_2 80:20 w/w	OCV	$R_e(R_1Q_1)(R_2Q_2)$	9.9 ± 0.2	4.2 ± 0.5	/	14.1 ± 0.7	5×10^{-5}
	After 1 CV cycle	$R_e(R_1Q_1)(R_2Q_2)Q_w$	2.0 ± 0.1	1.5 ± 0.5	/	3.5 ± 0.6	9×10^{-5}
	After 5 CV cycles	$R_e(R_1Q_1)(R_2Q_2)Q_w$	2.6 ± 0.1	0.9 ± 0.2	/	3.5 ± 0.3	2×10^{-5}
	After 10 CV cycles	$R_e(R_1Q_1)(R_2Q_2)(R_3Q_3)Q_w$	0.6 ± 0.2	4.2 ± 0.2	0.5 ± 0.1	5.3 ± 0.5	5×10^{-5}

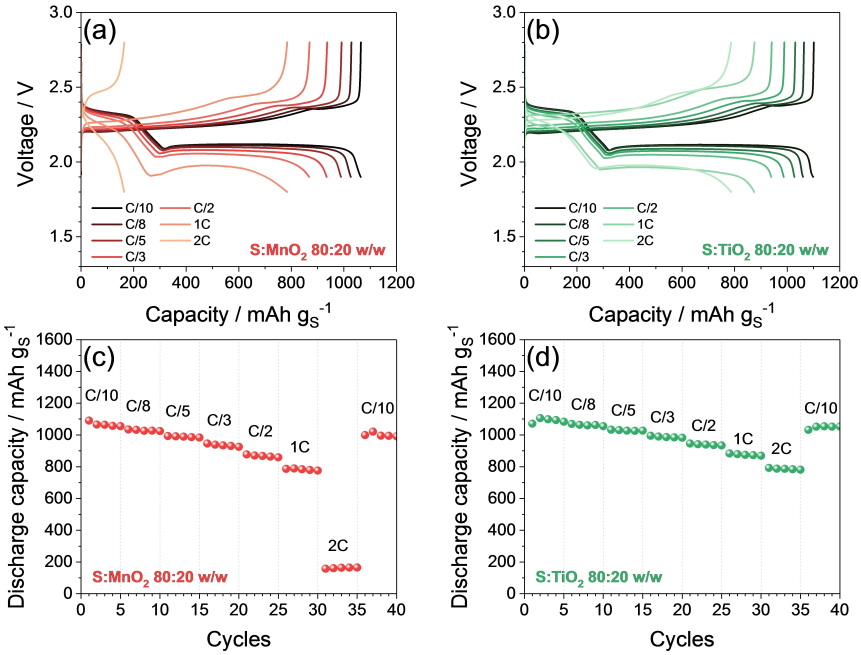

Figure 5. a, b) Voltage profiles and c, d) corresponding cycling trends collected upon rate capability tests of lithium cells with the configuration Li | DOL:DME, 1 mol kg^{-1} LiTFSI, 1 mol kg^{-1} $LiNO_3$ | cathode, employing either the a, c) S–MnO_2 or b,d) S–TiO_2 electrode. C-rates: C/10, C/8, C/5, C/3, C/2, 1C and 2C. Voltage ranges: 1.9–2.8 V from C/10 to C/2 and 1.8–2.8 V for 1C and 2C (1C = 1675 mA g$_S^{-1}$). Sulfur loading: 2 mg cm^{-2} (electrode geometric area: 1.54 cm^2). Electrolyte/sulfur (E/S) ratio: 15 µl mg^{-1}. Room temperature (25 °C). See the Experimental Section for acronyms.

and high coulombic efficiency. Furthermore, the corresponding voltage profiles displayed in Figure S4 in Supporting Information reveal the reversible Li–S conversion process and a low polarization of the discharge and charge processes at C/5 (Figure S4a, b) and 1C (Figure S4c, d) for S–MnO_2 and S–TiO_2, respectively. In particular, the sulfur composites exhibit similar behavior at C/5 (Figure 6a) with an initial capacity around 1120 mAh g$_S^{-1}$ retained for the 69% using S–MnO_2 and for 74% using S–TiO_2 upon the 120 cycles taken into account, and coulombic efficiencies of 99% after the initial stages of the tests. Instead, at 1C (Figure 6b) S–MnO_2 displays a slightly higher initial capacity with respect to S–TiO_2, that is, 1140 and 930 mAh g$_S^{-1}$ after the first cycle. However, S–MnO_2 evidences a faster capacity decay during the cycling test and shows a final capacity of 700 mAh g$_S^{-1}$ that corresponds to 61% of the initial value, while S–TiO_2 retains its capacity for 76%. Moreover, S–TiO_2 shows a relevant cell life of 400 cycles at the relatively high current rate of 2C (Figure 6c and Figure S4f), with an initial capacity of 850 mAh g$_S^{-1}$ retained for the 52% at the end of the test, and a final coulombic efficiency of 98%. Instead, S–MnO_2 shows at 2C a very poor electrochemical response (Figure S4e) in agreement with the rate capability outcomes discussed in Figure 5, thus further suggesting the faster reaction evolution promoted by the nanometric TiO_2 compared to the micrometric MnO_2, which may favor in turn an excessive lithium polysulfides retention. The small discrepancies of the delivered capacity values observed for rate capability tests (Figure 5) and the long-term cycling (Figure 6) may be due to slight difference in sulfur loading exploited by the S–MnO_2 and S–TiO_2 electrodes (i.e., 2.0 mg cm^{-2} for rate capability tests and between 1.5 and 2.0 mg cm^{-2} for long-term cycling tests) and to the adopted operative conditions. Indeed, the rate capability evaluation involves initial cycling at low C-rates that may influence kinetics and activation of the Li–S process (see experimental section). In summary, the galvanostatic tests in lithium cell suggest the direct physical combination of sulfur and metal oxides as viable synthetic strategy to achieve satisfactory cyclability of Li–S cells, and evidence the better response of S–TiO_2 with respect to S–MnO_2 due to the different morphology of the metal oxide additive.

The achievement of Li–S battery of practical interest certainly requires a high sulfur loading and a low electrolyte/sulfur (E/S) ratio to reach adequate energy density for a possible commercialization and enhance the cell characteristics compared to the state-of-the-art battery.[65–67] In this regard, Figure 7 displays additional galvanostatic tests performed on the Li–S cells employing electrodes with sulfur loading raised from about 2 mg cm^{-2} to about 5 to 6 mg cm^{-2} (referred to electrode geometric area) and E/S ratio in the cell lowered from 15 µl mg^{-1} to 10 µl mg^{-1} with respect to the tests reported above (Figure 5 and Figure 6). The measurements are carried out at a C-rate of C/5, which corresponds to a current density approaching 2 mA cm^{-2}, with a sulfur loading of 5.4 mg cm^{-2} for S–MnO_2 and 5.8 mg cm^{-2} for S–TiO_2. The resulting voltage profiles reveal reversible and lowly polarized discharge for both S–MnO_2 (Figure 7a) and S–TiO_2 (Figure 7b), and a charge processes exhibiting well-defined plateaus for the conversion of lithium polysulfides to Li and S. Interestingly, the discharge profiles in Figure 7a and b show a sloped trend that may be ascribed to the hindering of the Li^+ diffusion at the electrode/

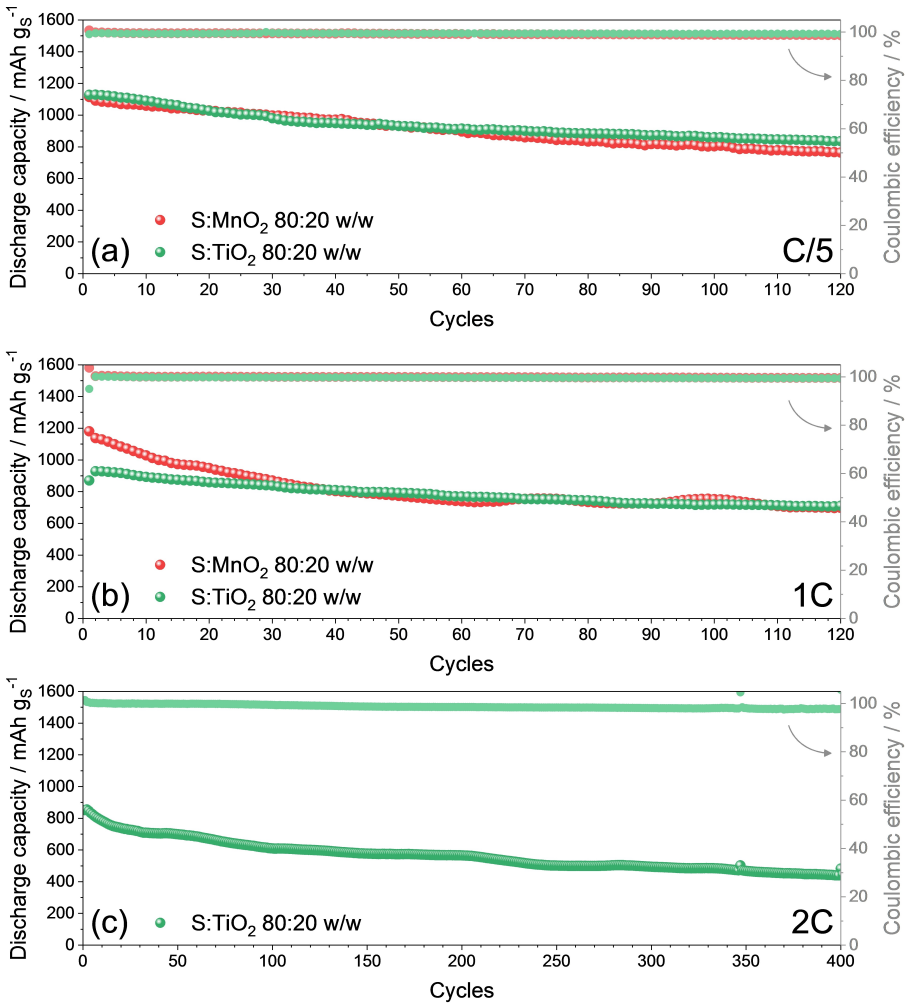

Figure 6. Trends of the prolonged galvanostatic cycling tests performed on lithium cells with the configuration Li | DOL:DME, 1 mol kg^{-1} LiTFSI, 1 mol kg^{-1} $LiNO_3$ | cathode, employing either S–MnO_2 (red) or S–TiO_2 (green) electrodes at the current rates of a) C/5, b) 1C and c) 2C (the latter only for S–TiO_2). Voltage ranges: 1.9–2.8 V for C/5 and 1.8–2.8 V for 1C and 2C. Sulfur loading: 1.5–2 mg cm^{-2} (electrode geometric area: 1.54 cm^2). Electrolyte/sulfur (E/S) ratio: 15 µl mg^{-1}. The corresponding voltage profiles are reported in Figure S4 in the Supporting Information. Room temperature (25 °C). See the Experimental Section for acronyms.

electrolyte interphase caused by the relevant sulfur content and by the relatively high current density.[60,68] Nevertheless, the Li–S cells deliver over 90 cycles with a coulombic efficiency approaching 100% after the initial stage (insets in Figure 7c and d) and steady state capacity exceeding 900 mAh g_S^{-1} that corresponds to about 5 mAh cm^{-2}, with a final value higher than 4.5 mAh cm^{-2}, as revealed by the cycling trends reported in Figure 7c for S–MnO_2 and Figure 7d for S–TiO_2. In particular, the S–MnO_2 electrode with a sulfur loading of 5.4 mg cm^{-2} exhibits an initial areal capacity of 5.9 mAh cm^{-2} (1090 mAh g_S^{-1}) which decreases to 5.3 mAh cm^{-2} (990 mAh g_S^{-1}) after 10 cycles and to 4.7 mAh cm^{-2} (865 mAh g_S^{-1}) after 90 cycles, while the S–TiO_2 electrode with a sulfur loading of 5.8 mg cm^{-2} delivers 5.7 mAh cm^{-2} (985 mAh g_S^{-1}), slightly decreasing to 5.6 mAh cm^{-2} (970 mAh g_S^{-1}) upon the first 10 cycles and to 4.7 mAh cm^{-2} (810 mAh g_S^{-1}) at the end of the test. In summary, both the sulfur composites demonstrate promising performance even in challenging conditions such as increased sulfur loading and limited E/S ratio, with a notable capacity retention attributed to the restraining action of the metal oxides into the cathode, and the limited polysulfides shuttle in the optimized cells.[69] In this regard, control electrodes exploiting exclusively sulfur were tested in lithium cells to evaluate the possible differences in the electrochemical behavior due to the absence of the metal oxides. Figure S5 (Supporting Information) displays the results of cycling tests carried out on Li cells employing the above sulfur control electrodes with loading of either 5.0 (Figure S5a, c) or 4.5 mg cm^{-2} (Figure S5b, d). Both the galvanostatic profiles (Figure S5a, b) and the related cycling trends (Figure S5c, d) reveal satisfactory initial performance comparable to those exhibited by the S–MnO_2 and S–TiO_2 electrodes (compare Figure S5 with Figure 7) which can be attributed to the electrode formulation adopted herein exploiting the carbon-cloth GDL support (see Experimental section). Indeed, this substrate is characterized by relevant porosity that ensures an optimal electric contact of the active material with the electrode structure and allows adequate kinetics of the Li–S conversion process.[60] However, both cells exhibit short cycle

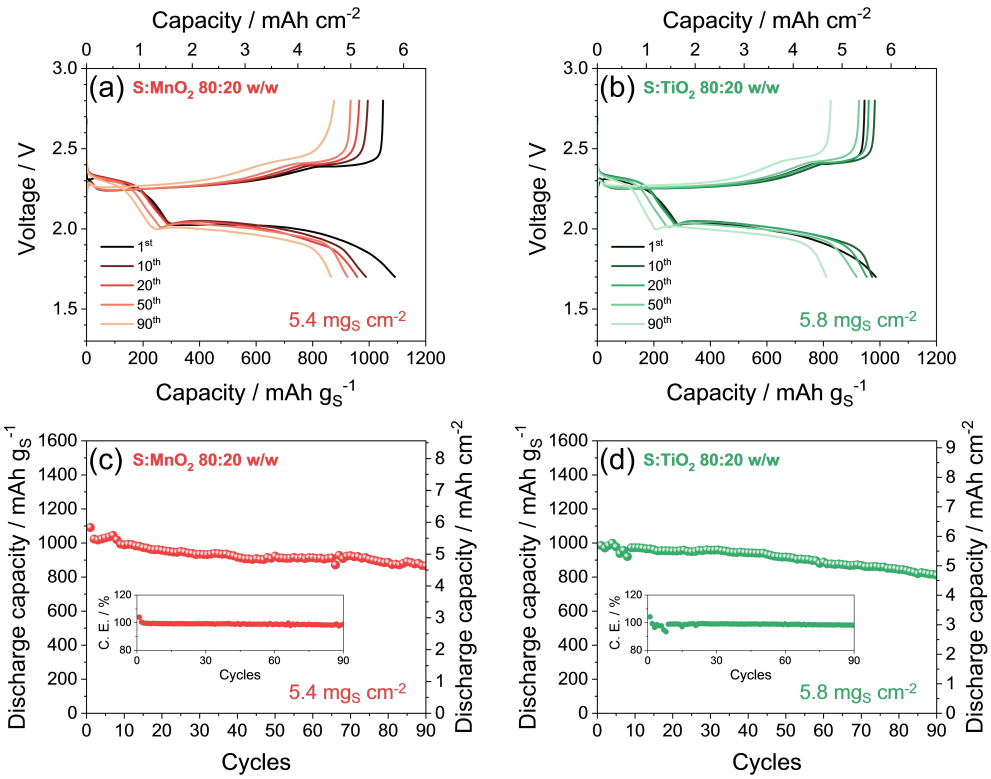

Figure 7. Galvanostatic cycling tests of lithium cells with the configuration Li | DOL:DME, 1 mol kg^{-1} LiTFSI, 1 mol kg^{-1} $LiNO_3$ | cathode employing either the a, c) S–MnO_2 or b, d) S–TiO_2 electrode with the relatively high sulfur loading of 5.4 and 5.8 mg cm^{-2}, respectively (electrode geometric area: 1.54 cm^2). In particular: a, b) voltage profiles and c, d) corresponding cycling trend of discharge/charge cycling at the constant current rate of C/5 (1C = 1675 mA g_S^{-1}) in the 1.7–2.8 V voltage range. Insets report corresponding Coulombic Efficiencies. Electrolyte/sulfur (E/S) ratio: 10 µl mg^{-1}. Room temperature (25 °C). See the Experimental Section for acronyms.

life and scarce rate capability due to several short circuits ascribed to massive formation of dendrites on the Li surface. This behavior is likely due to the massive diffusion of the lithium polysulfides during Li–S operation that reach and directly react with the lithium anode, thus favoring the formation of an irregular SEI, the uneven deposition of Li^+ ions during charge, and the shuttle process.[70] This phenomenon can be strongly mitigated by the addition of oxides that can retain the polysulfides and hinder their fast migration to the anode such as MnO_2 and TiO_2, thus allowing safe cycling even at a sulfur loading exceeding 5 mg cm^{-2} as demonstrated in Figure 7. These data may actually shed light on the various sustainable strategies for scaling-up efficient configurations of high-energy lithium-sulfur cells of practical interest.[42,59]

Conclusions

Composites synthetized by a simple pathway, composed of sulfur (80 wt.%) and either MnO_2 or TiO_2 powder (20 wt.%) were investigated for application in lithium battery. XRD measurements revealed a well-defined β and α phases for MnO_2 and TiO_2 powders, respectively, while SEM images displayed micrometric aggregates for MnO_2 and nanometric particles for TiO_2. Cyclic voltammetry (CV) and galvanostatic cycling tests performed in lithium cells shown modest side electrochemical activity for the MnO_2 electrode and fast deactivation of the TiO_2, and suggested a negligible contribution of the (de)insertion processes into the metal oxides to the overall capacity of the lithium-sulfur conversion reaction. Moreover, electrochemical impedance spectroscopy (EIS) carried out upon galvanostatic tests of the oxides in lithium cell exhibited a decrease of the electrode/electrolyte interphase resistance by cycling, thus accounting for formation of a stable solid electrolyte interphase (SEI) and confirming the applicability of MnO_2 and TiO_2. XRD and SEM-EDS analyses of the S–MnO_2 and S–TiO_2 composites exhibited the retention of the oxides structure and morphology, the absence of significant impurities and the homogeneous distribution of the metal oxide in the sulfur matrices. Furthermore, CV measurements of Li | S–MnO_2 and Li | S–TiO_2 cells evidenced a reversible, stable and lowly polarized Li–S conversion process characterized by two separated discharge signals at 2.28 and 2.0 V *vs.* Li^+/Li, and a broad charge double-signal between 2.3 and 2.5 V *vs.* Li^+/Li, thus excluding side electrochemical activity of MnO_2 and TiO_2. The voltammograms also revealed an *activation* of the Li–S process suggested by the shift of the discharge signal from 2.28 V *vs.* Li^+/Li to values exceeding 2.3 V *vs.* Li^+/Li, and the remarkable decrease of the electrode/electrolyte interphase resistance confirmed by EIS carried out upon CV. In particular, the resistance values of 24 Ω and 14 Ω measured at the OCV condition for the Li | S–MnO_2 and Li | S–TiO_2 systems, respectively, decreased to about 6 and

5 Ω after 10 CV cycles. Moreover, the EIS data revealed a Warburg-type Li^+ diffusion for the S–TiO_2 at the charged state, and a blocking-electrode trend for S–MnO_2, as likely ascribed to the different morphology of the two oxides in the composites which also influenced their cycling behavior. Indeed, rate capability tests displayed an efficient Li–S conversion process according with the CV data for the two sulfur composites from C/10 to 1C current, whilst only S–TiO_2 demonstrated suitable cycling at 2C. Moreover, S–TiO_2 exhibited better capacity retention, despite both the Li–S cells recovered over the 90% of the initial capacity when the current was lowered back to C/10. Prolonged galvanostatic tests confirmed the better response of the material using the nanometric TiO_2 and confirmed the kinetic limit related to the micrometric MnO_2. Hence, the Li|S–MnO_2 and Li|S–TiO_2 systems shown satisfactory trends over 120 cycles at C/5 and 1C rate, with a higher capacity retention for the S–TiO_2 electrode, particularly at 1C. Furthermore, only S–TiO_2 delivered an adequate capacity at 2C current, with a value of 850 mAh g_S^{-1} retained for over 50% after 400 discharge/charge cycles. In order to achieve more scalable Li–S cells, the sulfur loading in the electrode was increased up to 5.4 mg cm^{-2} for S–MnO_2 and 5.8 mg cm^{-2} for S–TiO_2, and the electrolyte/sulfur (E/S) ratio was limited to 10 µl mg^{-1}. The related galvanostatic tests at the current rate of C/5 (about 2 mA cm^{-2}) revealed initial areal capacity approaching 6 mAh cm^{-2} (as normalized to the electrode geometric area) and a notable final value of about 4.7 mAh cm^{-2} after 90 discharge/charge cycles, during which S–TiO_2 material exhibited once more a better retention. Therefore, the experimental outcomes of this work suggested the physical mixing pathway of sulfur and metal oxides as a practical process to achieve a composite for efficient Li–S battery, and evidenced the benefits of a nanometric morphology of the additive to allow fast reaction kinetics, long cycle life and satisfactory capacity retention.

Experimental Section

Metal Oxides

The structure and morphology of manganese (IV) oxide (MnO_2, ≥ 99%, Sigma-Aldrich) and titanium (IV) oxide (TiO_2, anatase, 99.8% trace metal basis, Sigma-Aldrich) powders were analyzed by X-ray diffraction (XRD) and scanning electron microscopy (SEM). The XRD patterns were acquired via a Bruker D8 Advance diffractometer equipped with a Cu–Kα source (8.05 keV) by performing scans between 10 and 90° (2θ) at 10 s $step^{-1}$ with a step size of 0.02°. A Zeiss EVO MA10 exploiting a tungsten thermionic electron source was used to collect SEM images, while TEM analyses were carried out though a Zeiss EM 910 microscope equipped with a tungsten thermoionic electron gun operating at 100 kV. Previous to TEM observation, the MnO_2 and TiO_2 samples were dispersed in water and sonicated through a Branson 3200 ultrasonic cleaner.

The electrochemical features of the MnO_2 and TiO_2 powders were preliminarily evaluated in lithium cell. MnO_2 and TiO_2 electrodes were prepared through solvent casting technique by using a doctor blade (MTI Corp.). The electrode slurries were prepared by mixing either MnO_2 or TiO_2 powders with Super P carbon (SPC, Timcal) conductive agent and polyvinylidene fluoride (Solef® 6020 PVDF) polymeric binder in the 80:10:10 weight ratio by using the *N*-methyl-2-pyrrolidone (NMP, Sigma-Aldrich) solvent. The slurries were cast on carbon-coated aluminum foils (MTI Corp.), heated at 70 °C for 3 hours to remove the NMP and subsequently cut into 10 mm-electrode disks which were dried overnight under vacuum at 110 °C to ensure the removal of water or solvent traces. The metal oxide electrodes were then transferred in an Ar-filled MBraun glovebox (H_2O and O_2 content below 1 ppm) to assemble lithium T-type cells. Three-electrode cells were obtained by combining a working metal oxide electrode (either MnO_2 or TiO_2) with two 10 mm-diameter lithium disks acting as counter and reference electrodes, respectively. Working and counter electrodes were separated by a glass fiber 10 mm-diameter disk (GF/B Whatman®) soaked with the electrolyte, that is, a solution of ethylene carbonate (EC) and dimethyl carbonate (DMC) mixed in the 1:1 volume ratio dissolving the lithium hexafluorophosphate ($LiPF_6$) conducting salt in concentration of 1 mol $dm_{solvent}^{-3}$. The electrolyte solution was directly purchased by Sigma-Aldrich (LP-30) and indicated as EC:DMC, 1 M $LiPF_6$. Two-electrode cells were prepared with the same method by excluding the lithium reference disk.

Cyclic voltammetry (CV) measurements were performed on three-electrode T-cells at the scan rate of 0.1 mV s^{-1} in the 1.9–3.8 V *vs.* Li^+/Li and 1.4–2.8 V *vs.* Li^+/Li potential ranges for MnO_2 and TiO_2, respectively. Galvanostatic cycling tests were carried out at the constant current rate of C/10 (1C = 308 mA g^{-1} for MnO_2 and 1C = 168 mA g^{-1} for TiO_2) in two-electrode lithium T-cells. A voltage limit of 1.9–3.8 V was used for the MnO_2 cell, while the TiO_2 one was cycled between 1.4 and 2.8 V. Electrochemical impedance spectroscopy (EIS) was performed on the two-electrode cells at the open circuit voltage (OCV) condition and upon 10 discharge/charge cycles at C/10 in the 500 kHz–100 mHz frequency range by using a 10 mV alternate voltage signal.

Electrolyte Preparation

The electrolyte for Li–S cells was prepared by mixing 1,3-dioxolane (DOL, anhydrous, contains ca. 75 ppm BHT as inhibitor, 99.8%, Sigma-Aldrich) and 1,2-dimethoxyethane (DME, anhydrous, 99.5%, inhibitor-free, Sigma-Aldrich) with a 1:1 weight ratio, and dissolving lithium bis(trifluoromethanesulfonyl)imide ($LiN(SO_2)_2(CF_3)_2$, LiTFSI, 99.95% trace metals basis, Sigma-Aldrich) as conductive salt and lithium nitrate ($LiNO_3$, 99.99% trace metals basis, Sigma-Aldrich) as passivating agent in the solvents mixture in a 1 mol $kg_{solvent}^{-1}$ concentration for each salt. Before employment, DOL and DME solvents were stored under molecular sieves (rods, 3 Å, size 1/16 in., Honeywell Fluka) until a water content lower than 10 ppm was achieved as determined by a Karl Fischer 899 Coulometer (Metrohm), while LiTFSI and $LiNO_3$ were dried for 2 days under vacuum at 110 °C. The electrolyte solution is indicated as DOL:DME, 1 mol kg^{-1} LiTFSI, 1 mol kg^{-1} $LiNO_3$.

An additional electrolyte containing lithium polysulfide for UV-vis analyses was prepared by adding 0.5 wt.% of Li_2S_8 to the DOL:DME, 1 mol kg^{-1} LiTFSI, 1 mol kg^{-1} $LiNO_3$ solution. The Li_2S_8 addition procedure is reported in a previous work.[71]

UV-vis analyses were carried out on the above DOL:DME, 1 mol kg^{-1} LiTFSI, 1 mol kg^{-1} $LiNO_3$, 0.5 wt.% Li_2S_8 samples at the pristine state, and upon 5 hours aging in contact with MnO_2 and TiO_2 powders in the 500–800 nm wavelength region. Absorption spectra were collected with an Agilent Cary 300 UV-Vis spectrophotometer at room temperature against a DOL:DME 1:1 *w/w* reference solution.

Sulfur Composites

Sulfur (≥95%, Riedel-de Haën) and either MnO_2 (≥99% Sigma-Aldrich) or TiO_2 (99.8% Sigma-Aldrich) powders were mixed in the 80:20 weight ratio by magnetic stirring at 125 °C until complete melting of sulfur and homogenization. The value of 125 °C was selected to ensure the complete melting of sulfur that starts at about 113 °C, and, at the same time, avoid possible evaporation with lowering of the sulfur content in the composite that may occur at higher temperatures. The sulfur-metal oxide composites were subsequently achieved by cooling down the mixture to room temperature, and grinding the resulting solid to get a fine powder. The composites, that is, S:MnO_2 80:20 w/w and S:TiO_2 80:20 w/w, are subsequently indicated by the acronyms S–MnO_2 and S–TiO_2, respectively.

Structure and morphology of the sulfur composites were investigated in the same conditions as for the bare metal oxides, that is, by XRD using Bruker D8 Advance diffractometer equipped with a Cu–Kα source (8.05 keV) scanning in the 10–90° 2θ range with a 10 s $step^{-1}$ scan rate and 0.02° step, and by SEM employing a Zeiss EVO MA10 using a tungsten thermionic electron source. Elements distribution analysis was carried out on the SEM images through energy dispersive X-ray spectroscopy (EDS) via a X-ACT Cambridge Instruments analyzer.

Thermogravimetric analyses (TGA) were carried out on S–MnO_2 and S–TiO_2 samples in the 25–800 °C temperature range under N_2 flow at a rate of 5 °C min^{-1} through a Mettler-Toledo TGA 2 instrument.

S–MnO_2 and S–TiO_2 electrodes were prepared through doctor blade (MTI Corp.) casting of slurries composed by the sulfur composite, SPC (Timcal), and PVDF (Solef®) with the 80:10:10 weight ratio dispersed in NMP (Sigma-Aldrich). The slurries composition allows a final sulfur content as high as 64 wt.% in the cathodes. Sulfur control electrodes were also prepared through a slurry composed by elemental sulfur, SPC and PVDF in the 80:10:10 weight ratio. The electrode slurries were coated on a carbon-cloth gas diffusion layer (GDL ELAT 1400, MTI Corp.), heated at 50 °C to remove the NMP, cut into 14-mm disks and dried under vacuum at 40 °C overnight. Subsequently, the electrodes were transferred in an Ar-filled MBraun glovebox (H_2O and O_2 content below 1 ppm) to assemble CR2032 coin-type cells (MTI Corp.) with 14 mm-diameter lithium disk anode separated from the sulfur cathode through a 16 mm-diameter Celgard 2400 foil soaked with the DOL:DME, 1 mol kg^{-1} LiTFSI, 1 mol kg^{-1} $LiNO_3$ electrolyte solution. The electrolyte/sulfur (E/S) ratios used for the electrochemical tests are specified below.

Electrochemical Measurements

CV, EIS and galvanostatic cycling measurements were carried out in lithium coin-cells exploiting sulfur cathodes, initially with an active material loading between 1.5 and 2 mg cm^{-2} (referred to the electrode geometric area of 1.54 cm^2) and an electrolyte to sulfur (E/S) ratio of 15 μl mg^{-1}. CV scans were performed in the 1.8–2.8 V *vs.* Li^+/Li potential range at 0.1 mV s^{-1}, while EIS was carried out at the OCV cell condition and upon voltammetry after 1, 5 and 10 cycles within the 500 kHz–100 mHz frequency range by applying a 10 mV alternate voltage signal. The rate capability of the cells was evaluated through galvanostatic tests at a C-rate increasing every 5 cycles, that is, C/10, C/8, C/5, C/3, C/2, 1C and 2C and decreasing back at C/10 after the 35th cycle, while the cells cycle life was investigated by prolonged cycling tests at C/5, 1C and 2C constant current rates (1C = 1675 mA g_S^{-1}). Discharge and charge processes were limited between 1.9 and 2.8 V from C/10 to C/2 and between 1.8 and 2.8 V at 1C and 2C. Additional galvanostatic cycling measurements were carried out at C/5 between 1.7 and 2.8 V in lithium cells employing sulfur cathodes with active material loading (referred to the electrode geometric area of 1.54 cm^2) of 5.4 and 5.8 mg cm^{-2} for S–MnO_2 and S–TiO_2, respectively and an E/S ratio of 10 μl mg^{-1}.

The sulfur control electrodes were tested in lithium coin-cells through galvanostatic cycling measurements at the constant rate of C/5 in the 1.7–2.8 V voltage range. The cells employed control electrodes with sulfur loading of 5.0 and 4.5 mg cm^{-2} and E/S ratio of 10 μl mg^{-1}.

All the CV and EIS measurements were carried out via a VersaSTAT MC Princeton Applied Research (PAR–AMETEK) analyzer, while a MACCOR series 4000 battery test system was employed for the galvanostatic cycling tests. The Nyquist plots recorded by EIS were analyzed with a Boukamp tool by applying the non-linear least squares (NLLS) fitting method to extrapolate equivalent circuits and resistance values.[53,54] Only fits exhibiting a χ^2 value of about 10^{-4} or lower were considered acceptable.

Acknowledgements

This project/work has received funding from the European Union's Horizon 2020 research and innovation programme Graphene Flagship under grant agreement No 881603. The authors also thank grant "Fondo di Ateneo per la Ricerca Locale (FAR) 2021", University of Ferrara, and the collaboration project "Accordo di Collaborazione Quadro 2015" between University of Ferrara (Department of Chemical and Pharmaceutical Sciences) and Sapienza University of Rome (Department of Chemistry). Open Access Funding provided by Universita degli Studi di Ferrara within the CRUI-CARE Agreement.

Conflict of Interest

The authors declare no conflict of interest.

Data Availability Statement

The data that support the findings of this study are available in the supplementary material of this article.

Keywords: S–MnO_2 · S–TiO_2 · Li–S batteries · scalability · long-life cycling

[1] N. O. Bonsu, *J. Cleaner Prod.* **2020**, *256*, 120659.
[2] X. Wang, Y. Ding, Y. Deng, Z. Chen, *Adv. Energy Mater.* **2020**, *10*, 1903864.
[3] S. Chen, F. Dai, M. Cai, *ACS Energy Lett.* **2020**, *5*, 3140.
[4] D. Di Lecce, R. Verrelli, J. Hassoun, *Green Chem.* **2017**, *19*, 3442.
[5] M. A. Rajaeifar, P. Ghadimi, M. Raugei, Y. Wu, O. Heidrich, *Resour. Conserv. Recycl.* **2022**, *180*, 106144.
[6] L. Carbone, S. G. Greenbaum, J. Hassoun, *Sustain. Energy Fuels* **2017**, *1*, 228.
[7] B. Scrosati, J. Hassoun, Y.-K. Sun, *Energy Environ. Sci.* **2011**, *4*, 3287.
[8] D. Di Lecce, V. Marangon, H.-G. Jung, Y. Tominaga, S. Greenbaum, J. Hassoun, *Green Chem.* **2022**, *24*, 1021.

[9] X. Ji, K. T. Lee, L. F. Nazar, *Nat. Mater.* **2009**, *8*, 500.
[10] A. Manthiram, Y. Fu, S.-H. Chung, C. Zu, Y.-S. Su, *Chem. Rev.* **2014**, *114*, 11751.
[11] H. Wang, Y. Yang, Y. Liang, J. T. Robinson, Y. Li, A. Jackson, Y. Cui, H. Dai, *Nano Lett.* **2011**, *11*, 2644.
[12] W. Ren, W. Ma, S. Zhang, B. Tang, *Energy Storage Mater.* **2019**, *23*, 707.
[13] L. E. Camacho-Forero, T. W. Smith, S. Bertolini, P. B. Balbuena, *J. Phys. Chem. C* **2015**, *119*, 26828.
[14] G. Zhou, E. Paek, G. S. Hwang, A. Manthiram, *Adv. Energy Mater.* **2016**, *6*, 1501355.
[15] S. S. Zhang, *Inorg. Chem. Front.* **2015**, *2*, 1059.
[16] M. Inagaki, M. Toyoda, Y. Soneda, T. Morishita, *Carbon* **2018**, *132*, 104.
[17] L. Xiao, Y. Cao, J. Xiao, B. Schwenzer, M. H. Engelhard, L. V. Saraf, Z. Nie, G. J. Exarhos, J. Liu, *Adv. Mater.* **2012**, *24*, 1176.
[18] G. Zhou, H. Tian, Y. Jin, X. Tao, B. Liu, R. Zhang, Z. W. Seh, D. Zhuo, Y. Liu, J. Sun, J. Zhao, C. Zu, D. S. Wu, Q. Zhang, Y. Cui, *Proc. Natl. Acad. Sci. USA* **2017**, *114*, 840.
[19] Z. Sun, J. Zhang, L. Yin, G. Hu, R. Fang, H.-M. Cheng, F. Li, *Nat. Commun.* **2017**, *8*, 14627.
[20] Y. Zheng, S. Zheng, H. Xue, H. Pang, *J. Mater. Chem. A* **2019**, *7*, 3469.
[21] W. Chen, T. Lei, T. Qian, W. Lv, W. He, C. Wu, X. Liu, J. Liu, B. Chen, C. Yan, J. Xiong, *Adv. Energy Mater.* **2018**, *8*, 1702889.
[22] A. Vizintin, R. Guterman, J. Schmidt, M. Antonietti, R. Dominko, *Chem. Mater.* **2018**, *30*, 5444.
[23] I. Gracia, H. Ben Youcef, X. Judez, U. Oteo, H. Zhang, C. Li, L. M. Rodriguez-Martinez, M. Armand, *J. Power Sources* **2018**, *390*, 148.
[24] V. Marangon, D. Di Lecce, L. Minnetti, J. Hassoun, *ChemElectroChem* **2021**, *8*, 3971.
[25] S. S. Zhang, *Electrochim. Acta* **2012**, *70*, 344.
[26] H. Zhang, G. G. Eshetu, X. Judez, C. Li, L. M. Rodriguez-Martínez, M. Armand, *Angew. Chem. Int. Ed.* **2018**, *57*, 15002.
[27] A. Rosenman, R. Elazari, G. Salitra, E. Markevich, D. Aurbach, A. Garsuch, *J. Electrochem. Soc.* **2015**, *162*, A470.
[28] Y.-S. Su, A. Manthiram, *Nat. Commun.* **2012**, *3*, DOI 10.1038/ncomms2163.
[29] G. Ma, Z. Wen, Q. Wang, C. Shen, P. Peng, J. Jin, X. Wu, *J. Power Sources* **2015**, *273*, 511.
[30] J. He, Y. Chen, A. Manthiram, *Energy Environ. Sci.* **2018**, *11*, 2560.
[31] W. Hu, Y. Hirota, Y. Zhu, N. Yoshida, M. Miyamoto, T. Zheng, N. Nishiyama, *ChemSusChem* **2017**, *10*, 3557.
[32] X. Liu, J.-Q. Huang, Q. Zhang, L. Mai, *Adv. Mater.* **2017**, *29*, 1601759.
[33] X. Liang, C. Hart, Q. Pang, A. Garsuch, T. Weiss, L. F. Nazar, *Nat. Commun.* **2015**, *6*, DOI 10.1038/ncomms6682.
[34] M. Li, Y. Dai, X. Pei, W. Chen, *Appl. Surf. Sci.* **2022**, *579*, 152178.
[35] X. Liang, L. F. Nazar, *ACS Nano* **2016**, *10*, 4192.
[36] A. Benítez, J. Amaro-Gahete, Y.-C. Chien, Á. Caballero, J. Morales, D. Brandell, *Renewable Sustainable Energy Rev.* **2022**, *154*, 111783.
[37] V. Marangon, C. Hernández-Rentero, M. Olivares-Marín, V. Gómez-Serrano, Á. Caballero, J. Morales, J. Hassoun, *ChemSusChem* **2021**, *14*, 3333.
[38] A. Y. S. Eng, V. Kumar, Y. Zhang, J. Luo, W. Wang, Y. Sun, W. Li, Z. W. Seh, *Adv. Energy Mater.* **2021**, *11*, 2003493.
[39] Y. Ye, F. Wu, S. Xu, W. Qu, L. Li, R. Chen, *J. Phys. Chem. Lett.* **2018**, *9*, 1398.
[40] Y. Ge, P. Chen, W. Zhang, Q. Shan, Y. Fang, N. Chen, Z. Yuan, Y. Zhang, X. Feng, *New J. Chem.* **2020**, *44*, 11365.
[41] J. Guo, S. Zhao, Y. Shen, G. Shao, F. Zhang, *ACS Sustainable Chem. Eng.* **2020**, *8*, 7609.
[42] A. Benítez, Á. Caballero, E. Rodríguez-Castellón, J. Morales, J. Hassoun, *ChemistrySelect* **2018**, *3*, 10371.
[43] D. Di Lecce, V. Marangon, W. Du, D. J. L. Brett, P. R. Shearing, J. Hassoun, *J. Power Sources* **2020**, *472*, 228424.
[44] A. Bolzan, C. Fong, B. Kennedy, C. Howard, *Aust. J. Chem.* **1993**, *46*, 939.
[45] I. Djerdj, A. M. Tonejc, *J. Alloys Compd.* **2006**, *413*, 159.
[46] D. Di Lecce, V. Gancitano, J. Hassoun, *ACS Sustainable Chem. Eng.* **2020**, *8*, 278.
[47] M. Zhang, N. Garcia-Araez, A. L. Hector, *J. Mater. Chem. A* **2018**, *6*, 14483.
[48] W. Il Jung, M. Nagao, C. Pitteloud, A. Yamada, R. Kanno, *J. Power Sources* **2010**, *195*, 3328.
[49] J. Lehr, W. M. Dose, M. Yakovleva, S. W. Donne, *J. Electrochem. Soc.* **2012**, *159*, A904.
[50] H. Tan, S. Wang, X. Lei, *J. Electrochem. Soc.* **2015**, *162*, A448.
[51] V. Aravindan, J. Gnanaraj, S. Madhavi, H.-K. Liu, *Chem. Eur. J.* **2011**, *17*, 14326.
[52] S. Lou, Y. Zhao, J. Wang, G. Yin, C. Du, X. Sun, *Small* **2019**, *15*, 1904740.
[53] B. Boukamp, *Solid State Ionics* **1986**, *20*, 31.
[54] B. Boukamp, *Solid State Ionics* **1986**, *18–19*, 136.
[55] S. Wei, D. Di Lecce, R. Messini D'Agostini, J. Hassoun, *ACS Appl. Energ. Mater.* **2021**, *4*, 8340.
[56] X. Tao, J. Wang, C. Liu, H. Wang, H. Yao, G. Zheng, Z. W. Seh, Q. Cai, W. Li, G. Zhou, C. Zu, Y. Cui, *Nat. Commun.* **2016**, *7*, 11203.
[57] M. U. M. Patel, R. Demir-Cakan, M. Morcrette, J.-M. Tarascon, M. Gaberscek, R. Dominko, *ChemSusChem* **2013**, *6*, 1177.
[58] V. Marangon, J. Hassoun, *Energy Technol.* **2019**, *7*, 1900081.
[59] V. Marangon, D. Di Lecce, F. Orsatti, D. J. L. Brett, P. R. Shearing, J. Hassoun, *Sustain. Energy Fuels* **2020**, *4*, 2907.
[60] V. Marangon, D. Di Lecce, D. J. L. Brett, P. R. Shearing, J. Hassoun, *J. Energy Chem.* **2022**, *64*, 116.
[61] A. Benítez, P. Márquez, M. Á. Martín, A. Caballero, *ChemSusChem* **2021**, *14*, 3915.
[62] J. Xiao, J. Z. Hu, H. Chen, M. Vijayakumar, J. Zheng, H. Pan, E. D. Walter, M. Hu, X. Deng, J. Feng, B. Y. Liaw, M. Gu, Z. D. Deng, D. Lu, S. Xu, C. Wang, J. Liu, *Nano Lett.* **2015**, *15*, 3309.
[63] C. fringant, A. Tranchant, R. Messina, *Electrochim. Acta* **1995**, *40*, 513.
[64] X. Tao, J. Wang, Z. Ying, Q. Cai, G. Zheng, Y. Gan, H. Huang, Y. Xia, C. Liang, W. Zhang, Y. Cui, *Nano Lett.* **2014**, *14*, 5288.
[65] A. Bhargav, J. He, A. Gupta, A. Manthiram, *Joule* **2020**, *4*, 285.
[66] C.-S. Cheng, S.-H. Chung, *Batteries & Supercaps* **2022**, *5*, e202100323.
[67] S.-H. Chung, C.-H. Chang, A. Manthiram, *J. Power Sources* **2016**, *334*, 179.
[68] R. Fang, S. Zhao, P. Hou, M. Cheng, S. Wang, H.-M. Cheng, C. Liu, F. Li, *Adv. Mater.* **2016**, *28*, 3374.
[69] H. Wei, E. F. Rodriguez, A. S. Best, A. F. Hollenkamp, D. Chen, R. A. Caruso, *Adv. Energy Mater.* **2017**, *7*, 1601616.
[70] X. Xu, S. Wang, H. Wang, B. Xu, C. Hu, Y. Jin, J. Liu, H. Yan, *J. Energy Storage* **2017**, *13*, 387.
[71] D. Di Lecce, V. Marangon, A. Benítez, Á. Caballero, J. Morales, E. Rodríguez-Castellón, J. Hassoun, *J. Power Sources* **2019**, *412*, 575.

Manuscript received: April 6, 2022
Accepted manuscript online: April 25, 2022